

Flight Test Comparison of Gust Rejection Capability for Various Multirotor Configurations

Mark J. S. Lopez **Mark B. Tischler** **Ondrej Juhasz**
Aerospace Engineer Senior Scientist Aerospace Engineer
Aviation Development Directorate
CCDC Aviation & Missile Center
Moffett Field, CA, USA

Anthony Gong **Frank C. Sanders** **Jonathan Y. Soong** **Samuel J. Nadell**
Research Associate Senior Research Associate Program Specialist Software Engineer
San Jose State University Universities Space Research Association
Ames Research Center Ames Research Center
Moffett Field, CA, USA Moffett Field, CA, USA

ABSTRACT

Multirotor unmanned aerial systems (UAS) are prone to turbulent wind conditions and gust disturbances. Improving gust rejection performance is a critical technology to enable multirotor UAS operations in highly turbulent conditions and has been a recent topic of interest for study. To better understand the impacts of configuration and demonstrate methodologies for improving gust rejection performance, three different multicopters (a quadcopter, hexacopter, and octocopter) were studied. For each vehicle, system identification was used to obtain models from flight data, flight control systems were designed to maximize gust rejection capability, and gust rejection performance was validated in flight using a physically simulated gusts and turbulence. An overview of the key developments and results are presented in this paper.

INTRODUCTION

Vertical takeoff and landing (VTOL) unammaned aerial systems (UAS) offer great flexibility in terms of ability to deploy and recover precisely in potentially small and confined environments. Additionally VTOL UAS offer precise positioning and position hold capabilities, enabling missions that conventional takeoff and landing (e.g., fixed-wing) UAS cannot achieve. However, VTOL UAS are prone to turbulent wind conditions and gust disturbances which can greatly diminish precise positioning capabilities. Improving gust rejection performance is a critical capability to enable UAS operations and has been a topic of recent interest.

Prior UAS Gust Rejection Work

Zarovy et al performed a set of indoor flight experiments using a coaxial helicopter Micro Air Vehicle (MAV) and simulated realistic wind environments from fan wall (Ref. 1). Hover, foward flight, and rooftop landing were explored, and it was

found that MAV flight control performance was severely degraded in all of the windy conditions studied. It was concluded that significant improvements in flight control design and gust rejection techniques were critical to enable safe operation in turbulent environments.

Bristeau et al derived a simple a flight dynamics simulation for a quadrotor UAS including propeller aerodynamics (Ref. 2). The simulation model was used to study the effects of center of gravity location and propeller flexibility on the stability and gust rejection capability. They concluded that propeller flexibility was important for accurately determining stability and gust rejection characteristics.

Whidborne and Cooke studied effects of tilt for multirotor UAS (Ref. 3) using simulation models. They found that while positive tilt (tilt inwards) can improve static stability, negative tilt (tilt outwards) can greatly improve gust rejection properties at the cost of some loss in static stability. This negative tilt is effectively similar to anhedral and associated gust rejection properties in fixed wing aircraft such as the Harrier.

Significant work from the University of Maryland has focused on the development and experimental validation of onboard flow sensing devices (Ref. 4). Such devices can be used on UAS to sense environmental wind conditions and improve flight control performance. Shrestha et al used an onboard flow sensing device on cyclocopter UAV to study gust rejection capability of a cyclocopter (Ref. 5). Shrestha et al found that the thrust vectoring offered by a cyclocopter greatly im-

Presented at the Vertical Flight Society's 75th Annual Forum & Technology Display, Philadelphia, PA, USA, May 13–16, 2019. Copyright © 2019 by the Vertical Flight Society. All rights reserved. Distribution Statement A: Approved for public release; distribution is unlimited.

Disclaimer: thoughts, opinions, and conclusions are those of the authors and do not specifically represent those of the Department of Defense.

proved gust rejection capability. Craig et al presented flow sensing work for improving handling qualities in turbulence for a quadcopter (Ref. 6). Craig et al used system identification to obtain a linear model of a quadcopter, then used optimization to specifically meet a set of desired handling qualities specifications. Experimental results showed improvement in gust rejection capability using optimized controls with flow-sensed feedback.

von Frankenberg and Nokleby studied gust rejection capabilities of the “OmniCopter”: a novel multirotor concept with separate lifting and translating rotors which decouples translational and rotational controls. Experimental results with the OmniCopter showed that the additional translational-specific rotors improved gust rejection capabilities compared to a traditional planar multi-rotor configuration (Ref. 7).

Mansson and Stenberg developed design and simulation models which were used to study a variety of configurations for gust and turbulence rejection capabilities (Ref. 8). It was found that a Y-6 type configuration (3 arms with 2 coaxial propellers on each arm; 6 propellers in total) was the most beneficial specifically for gust rejection properties in forward flight.

The work presented herein develops methods to understand the impacts of multirotor configuration on gust rejection capability.

Program Background

The U.S. Army Combat Capabilities Development Command Aviation & Missile Center, Aviation Development Directorate (CCDC AvMC ADD) has been tasked by the Defense Advanced Research Projects Agency (DARPA) to investigate methods for improving gust rejection capabilities in multirotor UAS. The effort is focused on developing and flight test demonstrating technologies for flight dynamics modeling, gust response modeling, and optimization of gust rejection capabilities in hovering flight.

The techniques used here are based on prior work that has been demonstrated by CCDC AvMC ADD. Juhasz et al used system identification to obtain a bare-airframe and turbulence models of an Iris+ quadrotor (Ref. 9). Berrios et al used the identification results from Juhasz et al in a control system optimization effort that greatly improved the gust rejection capabilities (Ref. 10). The bare-airframe and turbulence models allowed Berrios to optimize flight controls performance in turbulence, specifying precise desired response bounds on attitude and position for a given level of turbulence. The performance-based control design approach from Berrios et al was also used by Juhasz et al to improve gust rejection capabilities on a tail-sitter UAS (Ref. 11).

The work herein uses the same performance-based control design approach from Berrios et al (Ref. 10). System identification was used to obtain bare-airframe and turbulence models. The models from system identification were then used for performance-based control design.

Scope of Work

Current and future UAS have high degrees of control redundancy and additional control authority, which may be useful for improving gust rejection capability. The gust rejection effort at CCDC AvMC ADD expands on prior UAS work to better understand the impacts of configuration and demonstrate methodologies for improving gust rejection performance. Three different multicopters (a quadcopter, hexacopter, and octocopter) were studied to demonstrate the effects of adding rotors (increasing control redundancy) on gust rejection capability and performance.

The work presented herein is an overview of the key developments and results of the gust rejection effort. There are four primary areas of interest that were explored in the effort: (1) a reconfigurable multicopter model was obtained to better understand the impact of configuration on flight dynamics and inherent gust rejection capability, (2) closed form turbulence models for each multicopter configuration were obtained, (3) performance-based flight control optimization was used to achieve the maximum gust rejection performance from each configuration, and (4) a gust wall was constructed to physically generate repeatable gusts and turbulence. The gust rejection capabilities for each configuration were validated and compared using flight test results with the gust wall.

SYSTEM IDENTIFICATION RESULTS

Three different multirotor configurations were constructed to evaluate the effect of configuration on gust rejection performance: a quadcopter, hexacopter, and octocopter. The quadcopter, hexacopter, and octocopter vehicles were built using common parts, with the primary difference among the configurations being the number and location of arms and rotors. Each vehicle has a hub-to-hub diagonal distance of 4.17 ft, with 1.5 ft diameter rotors. The quadcopter, hexacopter, and octocopter weights are 13.4, 15.7, and 18.1 lb respectively, and pictures of each vehicle are shown in Figure 1.

Each of the 3 vehicles were constructed, then the AutoTune functionality in ArduCopter (Ref. 12) was used to obtain a baseline flight control system for each vehicle. The baseline flight control system provided by ArduCopter was simply used to allow each vehicle to be flown so that flight data for system identification could be gathered. Once a model was obtained with system identification, an optimized flight control solution could be obtained which replaced the baseline flight controls from AutoTune.

Bare Airframe Identification

Frequency domain system identification techniques were used to identify state-space models from flight data for each configuration (Ref. 13). The basic approach is described in detail for the Iris+ quadcopter by Juhasz et al (Ref. 9), and was as follows: (1) the vehicle was excited using frequency sweeps, (2) bare-airframe control effector inputs and measured vehicle responses were recorded, (3) time history flight data was



(a) Quadcopter



(b) Hexacopter



(c) Octocopter

Fig. 1: Pictures of each multirotor vehicle

processed to obtain frequency responses, and (4) a state-space model which simultaneously captures frequency responses of all input-output pairs was identified, and (5) the state-space model was verified in the time domain using flight data dissimilar to the frequency sweeps used in obtaining the model.

It should be noted that for the system identification work herein, additional processes were used specifically to obtain contributions from individual rotors. The process for obtaining bare-airframe models with contributions from individual rotors is discussed by Lopez et al in Ref. 14. The key bare-airframe modeling results related to gust rejection capability are summarized herein.

Guidelines from Tischler and Remple are used for parameter reliability and model acceptability (Ref. 13) of the identified state-space models. Cramér-Rao bounds are within 20% and insensitivities are within 10% for all identified parameters indicating good reliability. Table 1 shows the average

and maximum cost functions for each configuration. All models have average cost functions $J_{ave} < 50$ (Ref. 13), indicating that overall each individual model was in excellent agreement to its corresponding flight data. Maximum cost functions are also displayed for each configuration and are all below 100 which indicates good accuracy for all model frequency responses compared with corresponding flight data.

Table 1: Cost Functions for Identified State Space Models.

Configuration	Average Cost Function	Maximum Cost Function
Quadcopter	40.8	89.9 (q/lon)
Hexacopter	45.5	98.4 (\dot{u}/lon)
Octocopter	27.5	61.2 (\dot{u}/lon)

Reconfigurable Model

The bare-airframe state space models serve 3 purposes: (1) design of performance-based flight controls to maximize gust rejection capability for the existing flight vehicles, (2) development of a reconfigurable multicopter flight dynamics model, and (3) identification of turbulence models (performance-based flight controls and identification of turbulence models will be discussed in subsequent sections). The reconfigurable model produces flight dynamics for a user-selectable number and location of rotors, allowing alternate configurations to be analyzed prior to physical construction and system identification.

The reconfigurable multicopter model is based on identification of the “basic derivatives” as defined by McRuer (Ref. 15). The basic stability and control derivatives are in terms of force or moment, for example the basic pitch damping derivative has units of $[(ft - lb)/(rad/s)]$. This is in contrast to standard dimensional derivatives, which are in terms of acceleration, for example the standard dimensional pitch damping derivative has units of $[(rad/s^2)/(rad/s)] = [1/s]$. For clarity, the standard dimensional derivatives can be obtained by dividing the basic derivatives with the appropriate mass or inertia term. For example, standard dimensional pitch damping is obtained by dividing basic pitch damping by pitch inertia:

$$M_{q,dimensional} = M_{q,basic}/I_{yy} \quad (1)$$

The standard dimensional derivatives are normally used in state space flight dynamic model identification. The basic derivatives are independent of mass and inertia, and were used in the reconfigurable model in order to separate the effects of inertia from aerodynamic effects.

The reconfigurable multicopter model was derived from quadcopter and octocopter flight identified models. A model was extracted for the hexacopter configuration, however this data was only used in validation of the reconfigurable model, not in the reconfigurable model development. The reconfigurable model is developed by producing a trend-line fit between each

individual state space term of the quadcopter and octocopter identified models. Linear least-squares fits were used for quadcopter and octocopter state-space parameters that vary linearly with the number of rotors or rotor placement (e.g. weight, inertia, heave damping, etc.). Step-function fits were used for parameters that did not vary linearly with the number of rotors or rotor placement.

Figure 2 shows the basic pitch control derivative for an individual motor. The basic pitch control derivatives are for motors that have been relocated to be 1 ft from the vehicle center of gravity to account differences in rotor placement and resulting moment arm. Basic control power for an individual motor is shown in terms of moment [ft-lb] per motor input command [PWM]. The dashed line indicates the step-function fit used in the reconfigurable model (RM Fit). The red “x”, black upward facing triangle, and blue circle indicate the identified pitch control derivative for an individual motor for the quadcopter (Quad ID), hexacopter (Hexa ID), and octocopter (Octo ID) respectively. The error bars correspond to $1\sigma = 68\%$ confidence bounds based on Craemér-Rao bounds. The downward facing magenta triangle indicates the pitch control derivative for the hexacopter based on the reconfigurable model (Hexa RM) and lies directly on top of the directly identified hexacopter pitch control derivative (Hexa ID), indicating near perfect agreement between the reconfigurable model and directly identified hexacopter validation data.

For configurations where the number of rotors is less than 8, each motor has the same control power as an individual motor from the quadcopter. For configurations where the number of rotors is 8 or more, each motor has the same control power as an individual motor from the octocopter. Figure 2 shows a significant reduction (-10%) in individual motor control power between when the number of rotors is increased from 6 to 8. Changes in mass, inertia, geometry (rotor number and placement) are explicitly captured as terms in the reconfigurable model, and dynamics for individual control effectors (motors+fans) were directly identified and verified to be linear using a separate motor test stand. Thus, the only remaining physical source that can cause the reduction in individual motor control power is *aerodynamic interference due to*

the decrease in rotor spacing; rotors become physically close enough that aerodynamic interference occurs and significantly impacts flight dynamic response.

Total dimensional pitch control power for the reconfigurable model is shown in Fig. 3 as computed by:

$$M_{\delta, total\ mixer} = \frac{\sum_{i=1}^n M_{\delta, individual} \times (Moment\ Arm)_i}{I_{yy}} \quad (2)$$

The summation is taken over all n rotors. Individual motor control power $M_{\delta, individual}$ follows the step-function from Fig. 2, and accounts for the aerodynamic interference effects. The moment arms for individual motors are simply a function of geometry based on the desired placement for individual rotors. Inertia I_{yy} is linear function of the number of rotors and the chosen geometry (placement of rotors). Total dimensional control power is shown in terms of vehicle angular acceleration [rad/s²] per mixer input command [PWM]. Each of the terms listed in Eqn. 2 are competing: adding rotors increases the total force or moment (increases total control power), but simultaneously can cause changes in rotor spacing and placement/moment arm which can increase inertia and aerodynamic interference (decreases total control power). Due to all factors combined, the obtained result was unexpectedly that the quadcopter vehicle actually has the largest total dimensional control power in pitch. Compared to the quadcopter, the hexacopter has significantly less total pitch control power. The octocopter has more total pitch control power compared to the hexacopter, but not as much as the quadcopter. As total control power is one of the primary factors in gust rejection capability (increasing total control power also improves gust rejection capability), adding more rotors can result in a net increase or decrease in total control power and gust rejection capability, which may contradict initial intuition.

Similar validations for all individual state space terms were performed between the hexacopter directly identified model and the hexacopter configuration from the reconfigurable model. All terms from the reconfigurable model based hexacopter were within the 1-standard deviation error bounds from

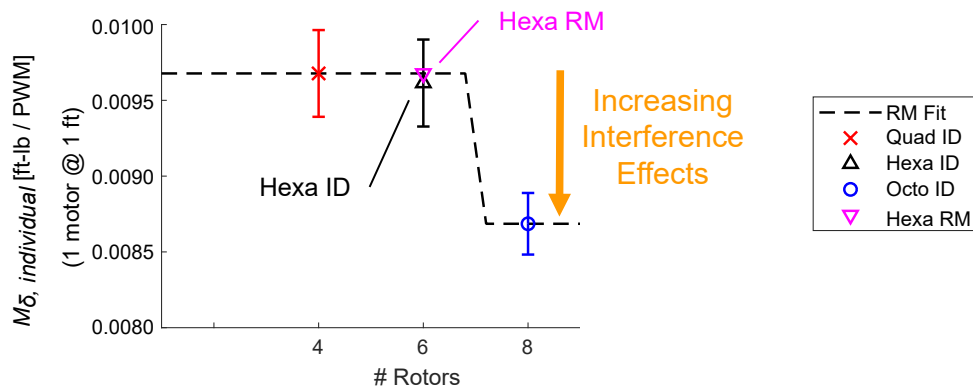


Fig. 2: Pitch control power for an individual motor (basic derivative).

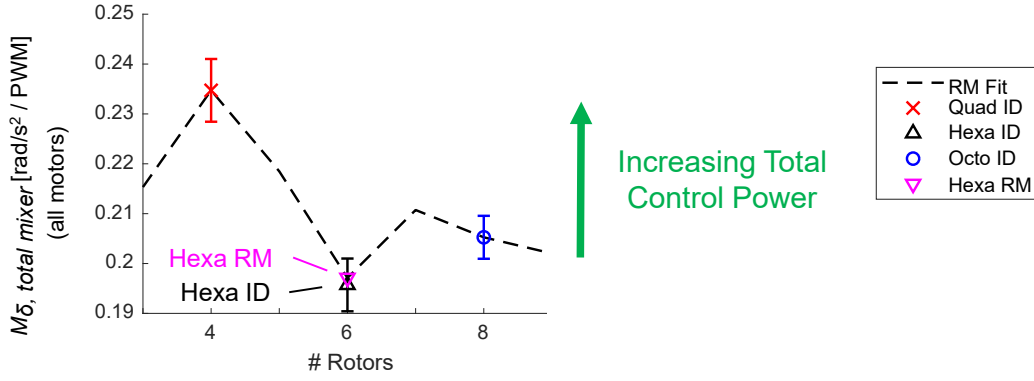


Fig. 3: Total pitch control power for reconfigurable model (dimensional derivative).

the directly identified hexacopter model, validating that the reconfigurable model is able to predict individual terms within the accuracy of the directly identified hexacopter model. Similarly, frequency response and time responses were also validated for the reconfigurable model with the hexacopter flight data, indicating that the reconfigurable model accurately tracks the complete vehicle responses and overall gust rejection capability.

Turbulence Model Identification

To maximize each aircraft's performance in turbulence, a Control Equivalent Turbulence Input (CETI) turbulence model was developed for each configuration. The CETI inputs are injected into the mixer input and cause the aircraft response to match those of the measured responses to turbulence. The CETI approach was first developed for large manned-sized rotorcraft by Lusardi et al (Ref. 16), but has also been demonstrated and validated for quadrotor and tail-sitter UAS by Juhasz et al (Ref. 9, 11). The CETI model allows deterministic, repeatable turbulence to be simulated for flight control design as well as generating in-flight simulated turbulence.

The turbulence extraction and identification methodology aims to identify an equivalent control input (δ_t) which excites the aircraft similarly to real turbulence as obtained from flight data on a windy day. The concept is shown in block diagram form in Fig. 4 for the longitudinal axis, where the measured aircraft response (q_m) is driven by the commanded inputs (δ_c) as well as turbulence inputs (δ_t).

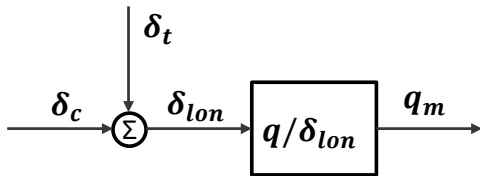


Fig. 4: Control Equivalent Turbulence Input (CETI) block diagram.

In equation form, the total measured pitch rate is:

$$q_m = \frac{q}{\delta_{lon}} (\delta_c + \delta_t) \quad (3)$$

Solving for the turbulence input gives:

$$\delta_t = \frac{\delta_{lon}}{q} q_m - \delta_c \quad (4)$$

The analysis was done completely in the frequency domain as in Refs. 9, 11. The time signals in Eqn. 4 become power spectral densities as shown in Eqn. 5.

$$G_{\delta_t \delta_t} = \left| \frac{\delta_{lon}}{q} \right|^2 G_{q_m q_m} - G_{\delta_c \delta_c} \quad (5)$$

It should be noted that signals from Eqn. 5 are in linear scale, not logarithmic scale.

As in Refs. 9, 11, a low-order transfer function of the CETI data is identified to form the actual turbulence model. For the quadcopter longitudinal CETI model, the following identified transfer function provided excellent results (cost $J = 12$), well within the excellent range for model accuracy. Due to the quadcopter symmetry, the longitudinal and lateral CETI models are constrained to be equal:

$$G_{\delta_{t_{lon}}}(s) = G_{\delta_{t_{lat}}}(s) = \frac{199.2}{(s^2 + 0.493s + 0.232)} \quad (6)$$

Similarly, for the quadcopter collective CETI model a low-order transfer function is identified to form the actual turbulence model. The following transfer function provided excellent results for collective (cost $J = 5$):

$$G_{\delta_{col}}(s) = \frac{26.25}{(s + 2.205)} \quad (7)$$

The transfer function model along with the data used in the identification for each turbulence level are shown in Fig. 5 for quadcopter longitudinal and lateral CETI models, and in

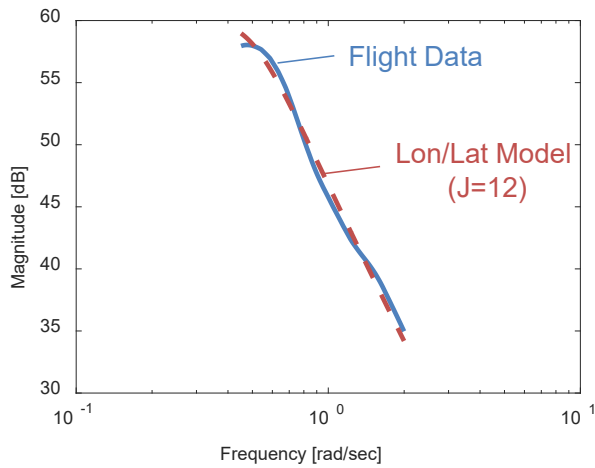


Fig. 5: Quadcopter CETI longitudinal and lateral models.

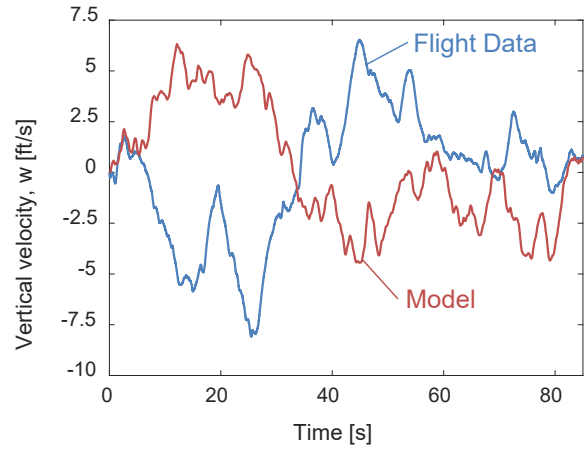


Fig. 7: Quadcopter CETI collective verification.

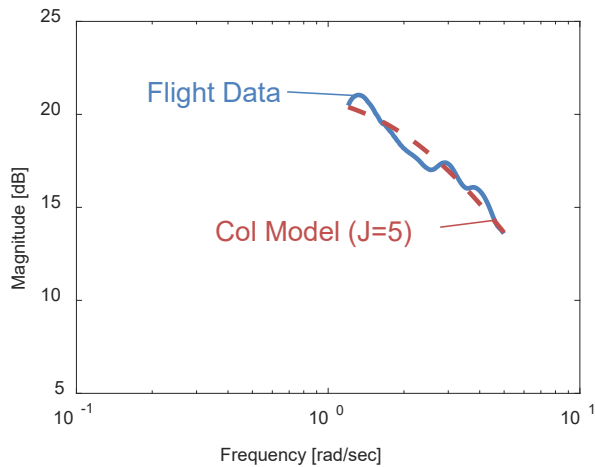


Fig. 6: Quadcopter CETI collective models.

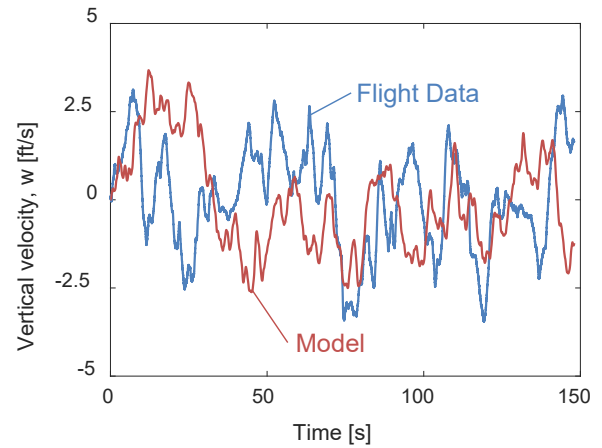


Fig. 8: Hexacopter CETI collective verification.

Fig. 6 for the quadcopter collective CETI model. The same methodology was used to extract similar models for the hexacopter and octocopter vehicles.

Figure 7 shows time domain validation of the quadcopter collective CETI model by comparing time histories from flight data and simulation. For both flight data and CETI model results in Fig. 7, there is no commanded input, thus the responses are entirely due to turbulence. Overall the CETI model generates very similar oscillations compared to flight data. It is important to note that the flight data and model time histories are not expected to line up, only that they have similar frequency content (similar amplitudes of oscillations). Similarly, Fig. 8 shows the hexacopter collective CETI model validation, and Fig. 9 shows the octocopter collective CETI model validation, both of which are compared to flight data with no commanded collective inputs. For each CETI validation figure, the CETI model generates similar oscillatory response compared to the corresponding flight data.

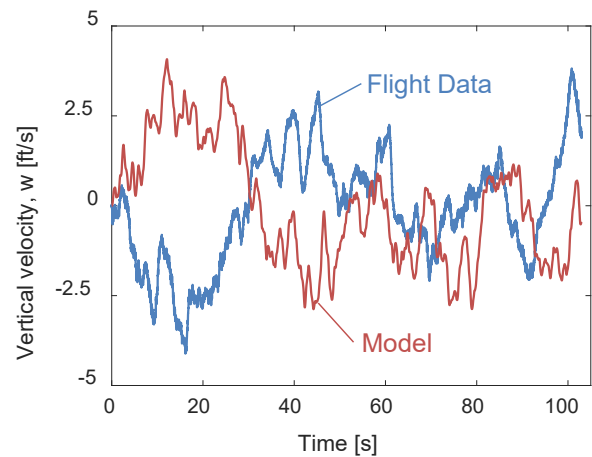


Fig. 9: Octocopter CETI collective verification.

Table 2: Specifications used for multicopter control design evaluation and optimization

Specification	Lateral/Longitudinal Axis	Heave Axis	Yaw Axis
	Lvl 1 Boundary Values	Lvl 1 Boundary Values	Lvl 1 Boundary Values
Eigenvalues	stable	stable	stable
Stability Margins	45° / 6 dB	45° / 6 dB	45° / 6 dB
Inner Loop Minimum Crossover	8 rad/sec	4 rad/sec	4 rad/sec
Disturbance Rejection Bandwidth	-	-	1.5 rad/sec
3 σ Attitude to CETI ¹	± 3 deg	-	-
3 σ Position to CETI ²	± 12 in	± 3 in	-

¹ Lat/lon axes optimized as part of inner-loop design margin optimization (DMO).

² Lat/lon axes optimized as part of outer-loop design margin optimization (DMO).

OPTIMIZED GUST REJECTION FLIGHT CONTROLS

Once flight dynamics models and turbulence models were obtained through system identification, a performance based flight controls approach was used to maximize gust rejection capabilities. The flight control design process used herein is the same performance based approach demonstrated by Berrios et al (Ref. 10) for a quadcopter, then by Juhasz et al (Ref. 11) for a tail-sitter.

The control system architecture uses an explicit model following architecture (Ref. 17) as depicted in Fig. 10. The longitudinal inner loop feedback is shown in Fig. 10a, which has a proportional-integral-derivative (PID) structure with an added lead to add phase margin around crossover and a lag to roll off and reject high frequency noise. The longitudinal outer loop feedback is shown in Fig. 10b, which feeds back position and velocity errors with respect to piloted commands and also includes a lead filter for additional phase margin. The full flight control block diagram is shown schematically in Fig. 10c, including the inner loop feedback, inner loop feed-forward (command, inverse, and equivalent delay), outer loop feedback, as well as the bare airframe dynamics obtained from system identification.

The flight control optimization was performed with the software tool CONDUIT (Ref. 17), where the objective of the optimization is to meet a desired level of vehicle stability and performance with the minimum amount of actuator usage. The stability and performance specifications which drove the optimization are listed Table 2, and include stable eigenvalues, 6 dB of gain margin, 45 deg of phase margin, minimum crossover, minimum disturbance rejection bandwidth, and $3\sigma = 99.7\%$ attitude and position response to a known level of turbulence.

The 3σ specifications from Berrios et al (Ref. 10) were used herein as initial guideline for achievable 3σ responses. The level 1 boundary values for crossover and disturbance rejection bandwidth specifications were determined by obtaining an optimized flight control solution that is stable and meets the 3σ specifications with the minimum actuator usage (actuator RMS). An optimized flight control solution which meets all

of the desired specifications with minimum actuator usage is known as the Pareto optimum solution and is known to be a good choice for flight control system design (Ref. 17). The resulting crossover and disturbance rejection bandwidth from the initial Pareto optimum solution were then used as the Level 1 requirements.

Once a Pareto optimum flight control solution was found with the initial design specifications, the desired level of vehicle response to CETI were then continually improved (response to turbulence is desired to be smaller) until the vehicle was no longer physically capable of meeting the set level of vehicle response while simultaneously satisfying the remaining specification requirements (e.g. stability or actuator limits). This process is referred to as performance-based design margin optimization (DMO), and was performed in a nested-loop fashion (Ref. 17): first the inner-loop attitude DMO is performed, then the outer-loop position DMO is performed.

The outer-loop DMO process is depicted for the octocopter in Figs. 11-15. Figure 11 shows the design specification for longitudinal x-position, where the baseline position response 3σ variation must be within ± 1 foot (at blue and magenta boundary). Once a baseline control solution was found that meets the desired ± 1 foot response, the design margin (DM) was then increased and the desired response became smaller (toward the blue region). Figure 12 shows the desired level of x-position 3σ variation moves from ± 12 inches in the baseline case (DM = 0%) down to ± 3.6 inches at DM = 70%. As the design margin increases (desired level of position response becomes smaller), the outer loop crossover frequency must increase as shown in Fig. 13. Similarly, as design margin increases, the amount of actuator usage in terms of RMS must also increase, as shown in Fig. 14. After DM = 70%, the amount of required actuator usage greatly increases past the physical capabilities of the actuator, and thus the maximum position hold gust rejection performance is achieved at 70% design margin corresponding to a 3σ position variation of ± 3.6 inches. The flight control designs are validated in flight as shown in Fig. 15, where the vehicle position response to simulated turbulence from the CETI model is shown with the semi-transparent shadow traces. The DM = 0% shown in red is able to hold a ± 12 inch box, and the DM = 70% shown

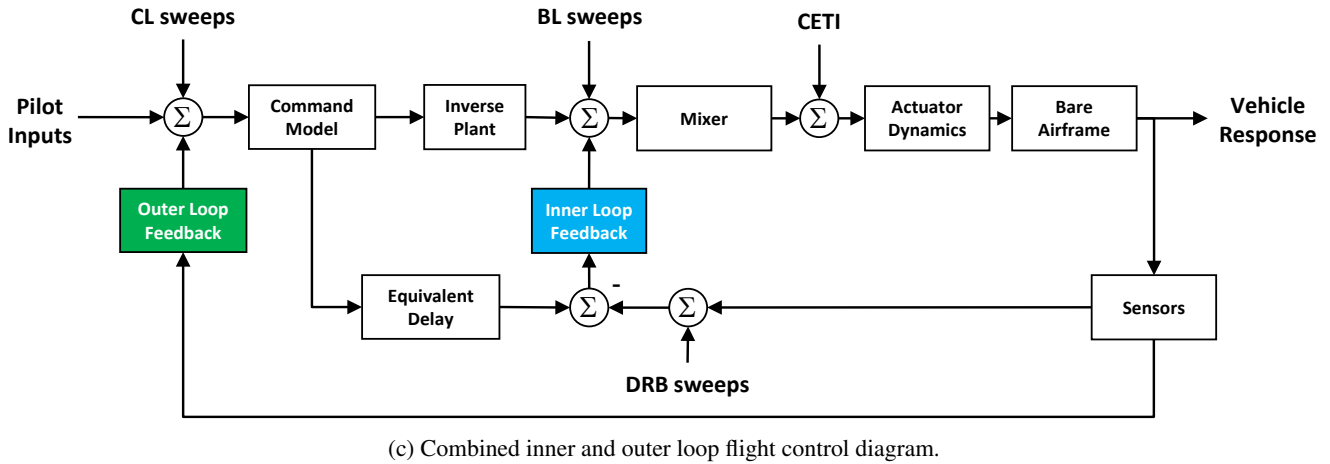
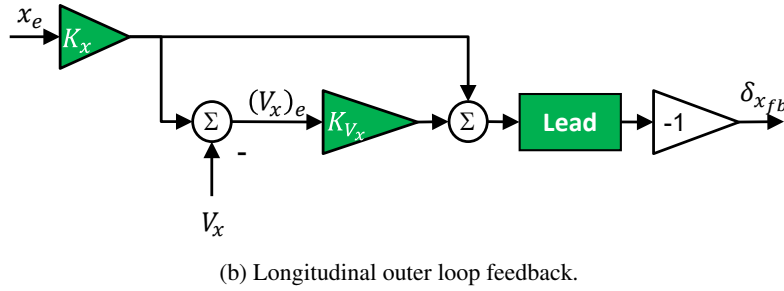
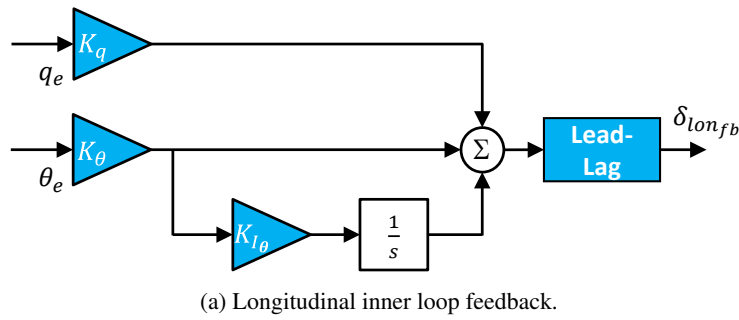


Fig. 10: Explicit model following flight control architecture.

in blue is able to hold a ± 3.6 inch box and corresponds to the maximum performance gust rejection flight controls.

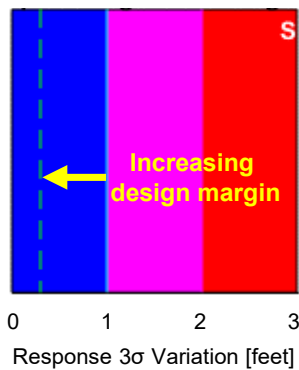


Fig. 11: Octocopter x-position 3σ design specification.

After the completion of the DMO process, the final control designs were validated in flight to ensure that the flight performance of the implemented designs matched the design specifications. Figure 16 shows the octocopter longitudinal closed-loop response from the CONDUIT design model (solid red) versus the measured flight data (dashed blue). The flight data tracks the CONDUIT design model magnitude and phase very well. Also, the coherence of the flight data is very high. A coherence value greater than 0.6 is considered acceptable, and a coherence of 1 is perfect. The coherence is above 0.6 and close to 1 for nearly the entire range of available flight data indicating that the response is very accurate (low random error) and is highly linear. Thus, the flight data validates that the octocopter longitudinal closed-loop response is implemented correctly and accurately tracks the CONDUIT design model.

Figures 17 and 18 show the octocopter longitudinal broken-loop and disturbance rejection responses respectively. The CONDUIT design model (solid red) is compared with the

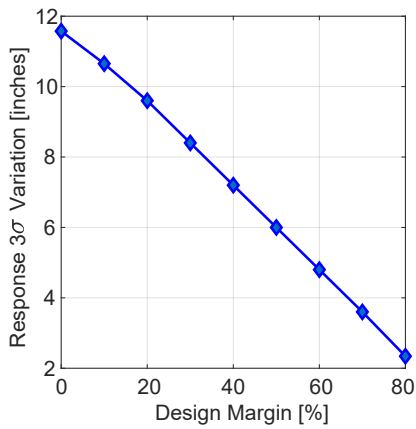


Fig. 12: Octocopter DMO, x-position 3σ .

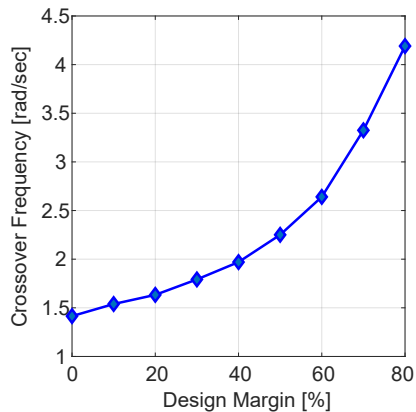


Fig. 13: Octocopter DMO, outer-loop δ_{lon} crossover frequency.

measured flight data (dashed blue). For both broken-loop and disturbance rejection responses shown, the flight data tracks the CONDUIT design model magnitude and phase very well with high coherence near crossover and disturbance rejection bandwidth frequencies respectively. Thus, the flight data validates that the octocopter longitudinal flight controls are implemented correctly, and that the actual in-flight broken-loop and disturbance rejection responses accurately track the CONDUIT design model. Validations for all axes and all vehicles were performed analogously (CONDUIT models were vali-

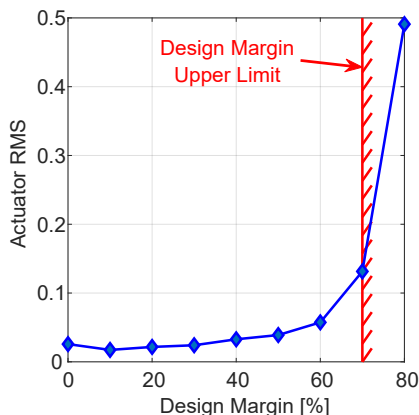


Fig. 14: Octocopter DMO, actuator RMS.

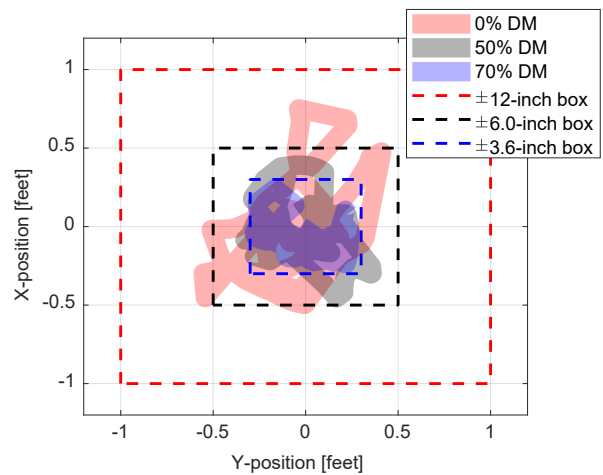


Fig. 15: Octocopter DMO, position-hold flight data with CETL.

dated with respective flight data) to ensure that the flight control designs were implemented correctly.

FLIGHT DATA VALIDATION

The performance-based flight control optimization process was performed independently on the quadcopter, hexacopter, and octocopter vehicles to achieve the best possible position hold performance for each of the individual configurations. Each of vehicles were then flight tested in the same turbulent wind conditions to evaluate their gust rejection capabilities.

Gust Wall

A gust wall was designed and constructed in order to physically generate repeatable wind conditions. The gust wall design is inspired by the WindShaper 1 (Ref. 18) Aerodrome Facility at the California Institute of Technology Center for Autonomous Systems and Technologies (Ref. 19) which uses a wall of fans to generate the desired wind conditions. A picture of the gust wall is shown in Fig. 19. The gust wall is composed of 12 individual fan cells, where each individual cell uses parts common to the air vehicles (propeller, motor, batteries, etc). This approach allows for a low cost, modular, lightweight, portable, and simple design.

The gust wall itself is about 7 feet wide by 7 feet tall. The wall produces mean winds in a single direction. Although the gust wall is capable of generating significant winds as far as 30 ft, the air vehicles are positioned 15 feet away from the gust wall as depicted in Fig. 20. The air vehicle positioning at 15 feet is far enough from the gust wall to mitigate safety issues, but is close enough that the wall can be run at lower power settings and still produce significant winds.

The winds generated by the gust wall were calibrated using an ultrasonic anemometer at 30, 60, and 100% power, as shown in Fig. 21. At maximum power, the gust wall is able to generate winds up to 30 mph at a distance of 10 ft, and winds up to 20 mph at a distance of 30 ft. The gust wall allows for

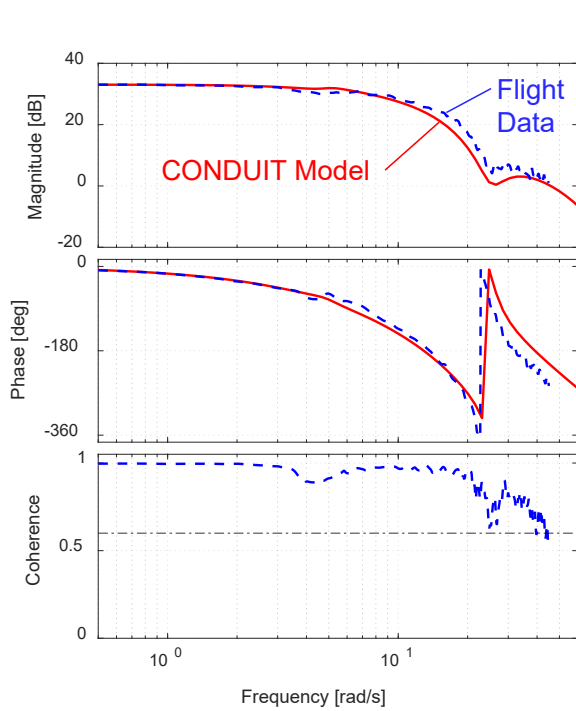


Fig. 16: Flight validation of octocopter longitudinal closed-loop response.

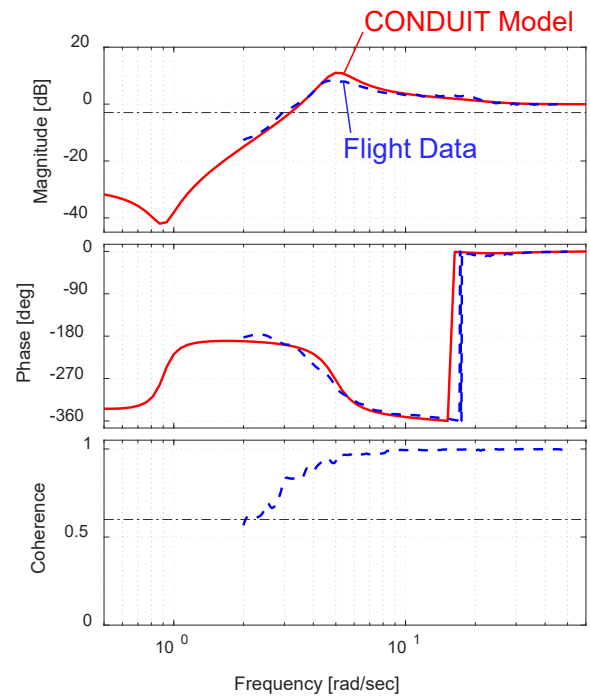


Fig. 18: Flight validation of octocopter longitudinal disturbance rejection response.

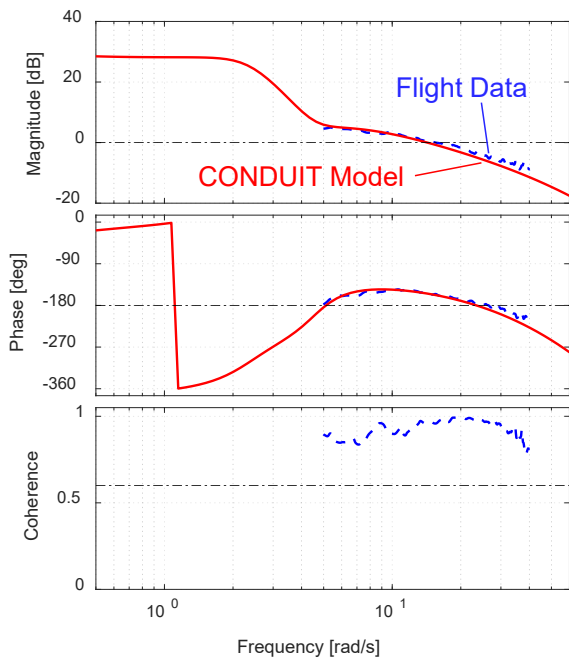


Fig. 17: Flight validation of octocopter longitudinal broken-loop response.



Fig. 19: Gust wall with 12 fan cells.

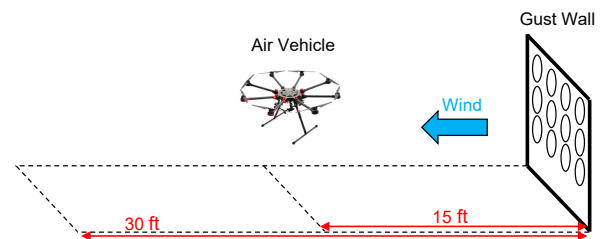


Fig. 20: Schematic drawing of flight testing setup.

wind conditions to be physically generated with consistency, allowing every vehicle to be flight tested with the same wind conditions. With individual control over the 12 fans, the gust wall can be programmed to produce any type of shaped winds: steady winds, transient winds (e.g., 1-cos type gust), wind gradients (e.g., low speeds from the bottom fans with high speeds from the top fans to produce the equivalent of a pitch gust), as well as randomized winds to inject simulated turbulence.

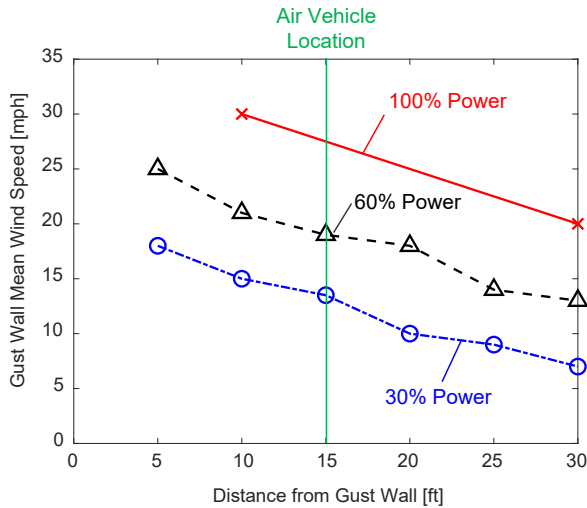


Fig. 21: Gust wall speed calibration.

It was found that the gust wall adds some additional turbulence, even when steady winds were commanded. Figure 22 show the power spectral densities measured from the gust wall at 17 mph (shown in the black solid line) compared with measurements of natural winds at 17 mph (dashed blue line). The power spectral densities show the turbulence levels in the mean wind direction as a function of frequency. Although both natural and gust wall generated winds had mean speeds of 17 mph and have the same general shape in power spectral densities, the gust wall overall has a higher power spectral density for the frequencies measured. This increase in power spectral density means that the gust wall has added turbulence inherent to the design of the gust wall itself. Nonetheless, the overall shape of the power spectral densities is similar meaning that the wall generated turbulence is similar to turbulence from natural winds, albeit at higher levels of turbulence for all frequencies measured.

The gust wall turbulence was calibrated as a function of the gust wall mean wind speeds as indicated in Fig. 23. Turbulence was measured as a single RMS value for each flow field direction. The direction aligned with the mean wind is labeled as u, the cross wind direction is labeled as v, and the vertical wind direction is labeled as w. RMS values for u,v, and w were computed for 3 different gust wall settings: 0 mph (gust wall is off, but ambient winds still exist), 10 mph, and 15 mph. The gust wall and testing occurs outdoors in a non-sterile environment; thus, at 0 mph there is still some very small turbulence (RMS of 1 mph or less) due to ambient air conditions. When the gust wall is brought to a mean speed

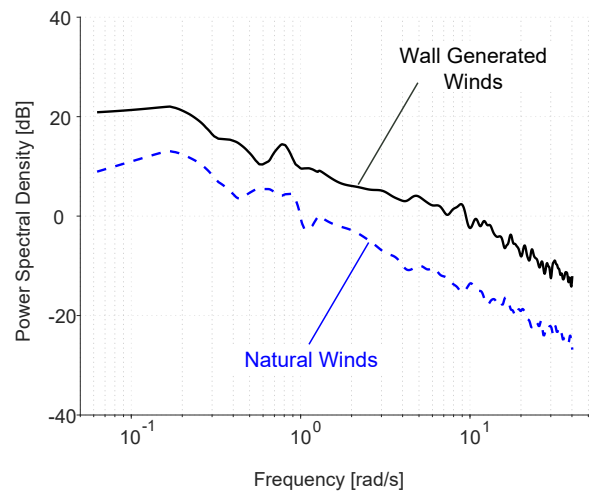


Fig. 22: Gust wall vs natural turbulence comparison, 17 mph mean wind.

of 10 mph, the absolute turbulence levels in each direction increase to 2.4 mph in u, 1.7 mph in v, and 1.5 mph in w. At a mean speed of 10 mph, the corresponding relative turbulence levels (expressed as a percentage of the mean speed, similar to Dryden turbulence levels) are 24% in u, 17% in v, and 15% in w. As the mean wind speed increases from 10 to 15 mph, the absolute turbulence levels in u doubles to 4.8 mph, with increases to 2.4 mph in v and 2.2 mph in w. The 15 mph relative turbulence levels are increased in u to 32%, but are nearly unchanged in v and w at 16% and 15% respectively. Thus, increased mean wind speeds corresponds to increased levels of absolute turbulence, which corroborates prior turbulence model parameterizations by by Lusardi et al (Ref. 16) and Juhasz et al (Ref. 11).

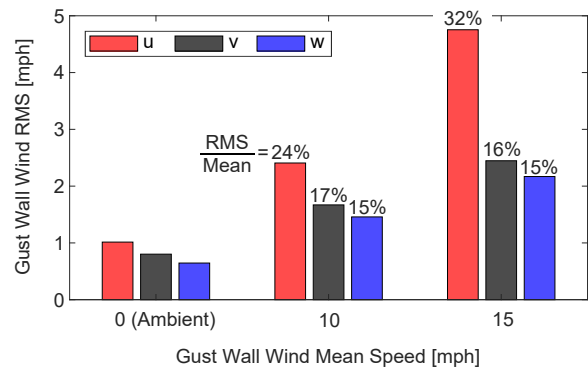


Fig. 23: Gust wall turbulence calibration.

Some additional insight can be gained by examining the RMS contributions from turbulence below and above the inner-loop crossover frequency ω_c . Figure 24 shows the power spectral densities at 17 mph in u,v, and w flow field directions, along with the representative inner-loop crossover frequency $\omega_c = 10 \text{ rad/s}$. Figure 25 shows the percentage contribu-

tions to RMS from turbulence below and above the inner loop crossover frequency of $\omega_c = 10 \text{ rad/s}$ from Fig. 24. For a crossover frequency of $\omega_c = 10 \text{ rad/s}$, 75% of the RMS in the mean wind direction u is below crossover. This corresponds to an initial guideline that 75% of the turbulence in u will be rejected for the associated wind conditions.

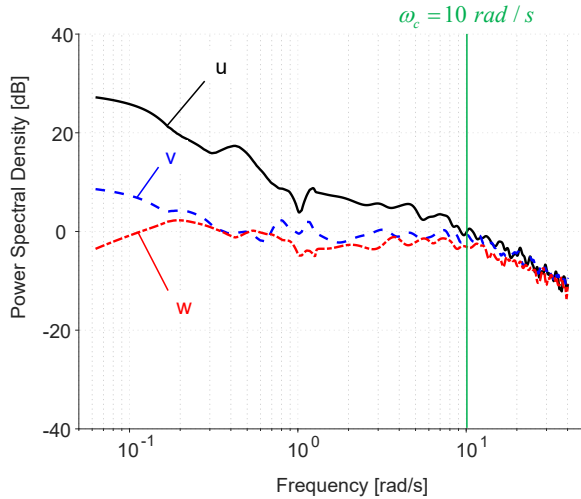


Fig. 24: Power spectral density of gust wall turbulence.

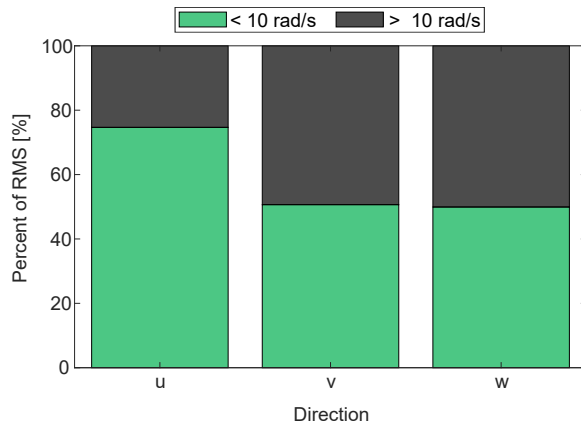


Fig. 25: RMS contributions with respect to crossover frequency.

The inverse of this type of analysis can also be used to determine initial flight control design requirements for a known set of wind and turbulence conditions. For a given level of desired turbulence rejection, one could compute the needed crossover frequency to achieve said level of turbulence rejection. For example, for a desired turbulence rejection level of 75% of RMS in the mean wind direction u , a crossover frequency $\omega_c = 10 \text{ rad/s}$ would yield 75% of the RMS in u to be below crossover, thus meeting the 75% desired turbulence rejection level. The benefit of this methodology is that only characterization of wind and turbulence conditions in-and-of itself are needed for the initial design requirements; there is no knowledge needed of the flight vehicle at all. This is in

contrast to a method demonstrated by Berrios et al (Ref. 10) which is a model based approach for determining flight control design requirements to reject an associated amount of turbulence, and requires accurate models of both turbulence and bare-airframe vehicle dynamics. While Berrios's method may yield a more detailed understanding of response characteristics, the methodology presented herein is advantageous for obtaining preliminary flight control design specifications prior to a flight vehicle itself being designed (such as in the preliminary design stage).

Flight Testing Results

Each vehicle was flown in winds generated by the gust wall. The position hold response to 15 mph winds (moderate winds) is shown in Fig. 26 for quadcopter, hexacopter, and octocopter vehicles as indicated by the semi-transparent shadow traces. Furthermore, the $2\sigma = 95\%$ bounds for each configuration are shown by the dashed circles. Note that the 2-sigma bounds are computed over all 15 mph records for each configuration, while the shadow traces are displayed only for a single record. Qualitatively it is clear that the hexacopter has the largest amount of deviation, as the black shadow traces the largest area, and the black dashed line has the largest diameter.

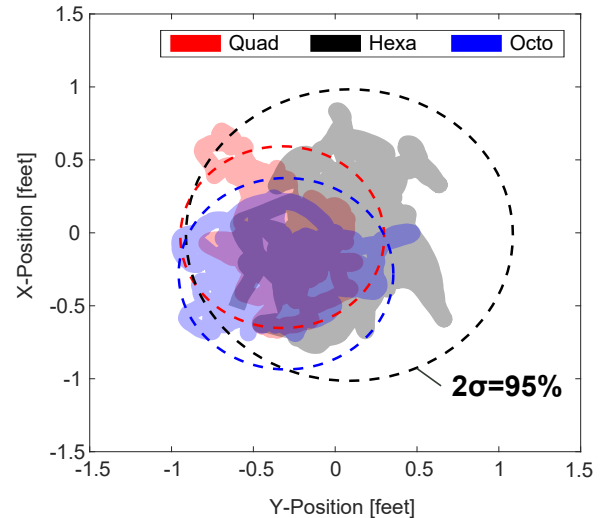


Fig. 26: Position hold in moderate winds (15 mph).

Figure 27 shows the standard deviations of each vehicle in position hold with varying levels of wind due to the gust wall. Low, low-moderate, and moderate winds correspond to 5, 10, and 15 mph winds respectively. Comparing the low, low-moderate, and moderate standard deviations for the quadcopter, as winds increase from 5, to 10, to 15 mph, the position standard deviations also increase from 2.3, to 3.0, to 3.7 inches respectively. As one would expect, the quadcopter has larger position standard deviations and worse position hold performance as wind and turbulence intensity levels increase. Similarly, the hexacopter position standard deviations also trend upward with increasing wind and turbulence intensity,

although the change in standard deviation per change in wind intensity is less when compared to the quadcopter. The octocopter actually has approximately the same position hold performance and standard deviation for each of the 3 wind and associated turbulence conditions examined. Thus, while the position hold performance for quad and hexacopter vehicles varies depending on the wind intensity, the octocopter position hold performance does not. The insensitivity of the octocopter position hold performance to wind magnitude is likely inherent to the larger inertia of the octocopter compared to the lighter quadcopter and hexacopter.

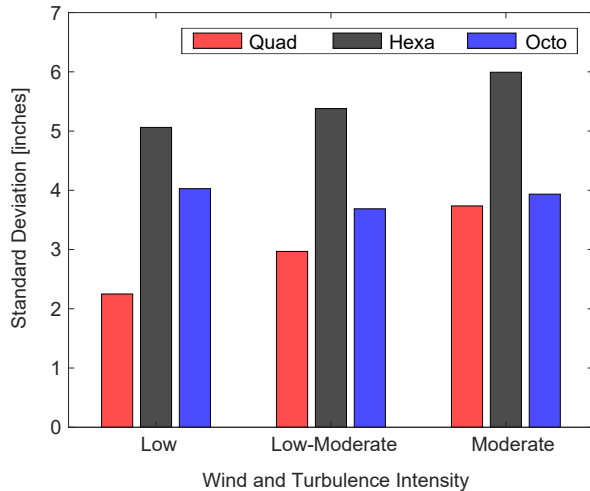


Fig. 27: Position standard deviation with varying winds.

For each wind condition, comparison of hexa versus quadcopter standard deviations shows that while the hexacopter has more rotors and is able to generate overall more force and moments, the changes in mass and inertia actually result in a net decrease in position hold and gust rejection capability. The octocopter is able to improve position hold and gust rejection capability when compared to the hexacopter, but the octocopter overall position hold and gust rejection capabilities are similar to that of the quadcopter in moderate wind. Thus, while adding rotors and arms can increase the total force (useful for increased payload, redundancy, and other reasons), the net effect on gust rejection capability is also dependent on resulting changes in mass and inertia. The gust rejection capability results from flight test corroborate the analysis of the gust rejection capability based on control power analysis of the reconfigurable model.

CONCLUSIONS

Three different multirotor configurations were used to evaluate the effect of configuration on gust rejection performance: a quadcopter, hexacopter, and octocopter. For each configuration, flight dynamics and turbulence models were obtained using system identification which enabled the design and flight testing of performance-based flight controls. Gust rejection capability was validated in flight using a gust wall and physically repeatable wind and turbulence conditions.

This work supports the following conclusions:

1. Individual rotor control power may be reduced when the number of rotor is increased. This is due to decreased rotor spacing which results in significant aerodynamic interference effects between rotors. A 10% reduction in individual rotor control power was observed for the octocopter in comparison to quadcopter and hexacopter identification results.
2. Performance-based flight control design produced the maximum gust rejection performance for the quadcopter, hexacopter, and octocopter configurations, with all configurations able to hold position within +/- 6 inches or better as validated by flight testing with the gust wall with up to moderate winds and turbulence.
3. Increasing the number of rotors increases both control power and inertia, which impact gust rejection ability in opposite ways. More control power improves gust rejection capability, while more inertia decreases gust rejection capability.
4. The hexacopter has more rotors and control redundancy, but less gust rejection capability when compared with the quadcopter. The octocopter has the most number of rotors of all configurations examined and has similar gust rejection capability to the quadcopter for moderate winds.

ACKNOWLEDGMENTS

This work was sponsored by the Defense Advanced Research Project Agency, Tactical Technology Office (DARPA TTO) under the Gust Rejection effort at the U.S. Army Combat Capabilities Development Command Aviation & Missile Center, Aviation Development Directorate (CCDC AvMC ADD), managed by Dr. Alexander M. G. Walan. The authors would like to thank the Gust Rejection team at DARPA TTO for their support. The authors would also like to thank Dr. Mark F. Costello for his support of the Gust Rejection effort at CCDC AvMC ADD.

REFERENCES

- ¹Zarovy, S., Costello, M. Mehta, A., Gremillion, G., Miller, D., Ranganathan, B., Humbert, J. S., and Samuel, P., "Experimental Study of Gust Effects on Micro Air Vehicles," AIAA Atmospheric Flight Mechanics Conference, 2-5 August 2010, Toronto, Ontario, Canada.
- ²Bristeau, P., Martin P., Salaun, E., and Petit, N., "The Role of Propeller Aerodynamics in the Model of a Quadrotor UAV," Proceeding of the European Control Conference 2009, Budapest, Hungary, August 23-26, 2009.
- ³Whidborne, J. F., and Cooke, A. K., "Gust Rejection Properties of VTOL Multirotor Aircraft," International Federation of Automatic Control, Control Conference Africa, Vol 50, Issue 2, Pg 175-180, 2017. DOI: 10.1016/j.ifacol.2017.12.032

⁴Yeo, D., Sydney, N., Paley, D., and Sofge, D., “Onboard Flow Sensing for Downwash Detection and Avoidance with a Small Quadrotor Helicopter,” AIAA Guidance, Navigation, and Control Conference, AIAA SciTech, January 2015.

⁵Shrestha, E., Yeo, D., Hrishikeshavan, V., Chopra, I., “Improved Gust Tolerance of a Cyclocopter UAV using Onboard Flow Sensing,” presented at the Vertical Flight Society 8th Biennial Autonomous VTOL Technical Meeting, Mesa, AZ, January 29-31, 2019.

⁶Craig, W., Lewis, J. T., Paley, D. A., “Stabilization of a Quadrotor in Wind with Flow Sensing: Linear Modeling and Control for Attitude and Position Hold,” presented at the Vertical Flight Society 8th Biennial Autonomous VTOL Technical Meeting, Mesa, AZ, January 29-31, 2019.

⁷von Frankenberg, F. and Nokleby, S., “Disturbance Rejection in Multi-Rotor Unmanned Aerial Vehicles Using a Novel Rotor Geometry,” Proceedings of the 4th International Conference of Control, Dynamic Systems, and Robotics, Toronto, Canada, August 21-13, 2017, Paper No. 130, DOI: 10.11159/cdsr17.130

⁸Mansson, C., and Stenbrg, D., “Model-based Design Development and Control of a Wind Resistant Multirotor UAV,” Masters Thesis, Lund University, Department of Automatic Control, ISRN LUTFD2/TFRT-5947-SE, June 2014.

⁹Juhasz, O., Lopez, M. J. S., Berrios, M. G., Berger, T., and Tischler, M. B., “Turbulence Modeling of a Small Quadrotor UAS Using System Identification from Flight Data,” presented at the Seventh AHS Technical Meeting on VTOL Unmanned Aircraft Systems, Mesa, AZ, January 24-26, 2017.

¹⁰Berrios, M. G., Berger, T., Tischler, M. B., Juhasz, O., and Sanders, F. C., “Hover Flight Control Design for UAS Using Performance-based Disturbance Rejection Requirements,” presented at the AHS International 73rd Annual Forum & Technology Display, Fort Worth, TX, May 9-11, 2017.

¹¹Juhasz, O., Tischler, M. B., and Won, H. “System Identification and Control Law Optimization Applied to the AeroVironment Quantixm™ Tail-Sitter UAS,” presented at the AHS International 74th Annual Forum & Technology Display, Phoenix, AZ, May 14-17, 2018.

¹²ArduPilot Dev Team, “AutoTune,” <http://ardupilot.org/copter/docs/autotune.html>

¹³Tischler, M. B. and Remple, R. K., *Aircraft and Rotorcraft System Identification: Engineering Methods with Flight Test Examples*, 2nd Edition, American Institute of Aeronautics and Astronautics, Inc., Reston, VA, 2012.

¹⁴Lopez, M. J. S., Tischler, M. B., Juhasz, O., Gong, A., and Sanders, F. C., “Development of a Reconfigurable Multi-copter Flight Dynamics Model From Flight Data Using System Identification,” presented at the Vertical Flight Society 8th Biennial Autonomous VTOL Technical Meeting, Mesa, AZ, January 29-31, 2019.

¹⁵McRuer, D. T., Graham, D., and Ashkenas, I., *Aircraft Dynamics and Automatic Control*, Princeton University Press, Princeton, NJ, 1973.

¹⁶Lusardi, J. A., Tischler, M. B., Blanken, C. L., and Labows, S. J., “Empirically Derived Helicopter Response Model and Control System Requirements for Flight in Turbulence,” *Journal of the American Helicopter Society*, July 2004, pp. 340-349.

¹⁷Tischler, M. B., Berger, T., Ivler, C. M., Mansur, M. H., Cheung, K. K., and Soong, J. Y., *Practical Methods for Aircraft and Rotorcraft Flight Control Design: An Optimization-Based Approach*, American Institute of Aeronautics and Astronautics, Inc., Reston, VA, 2017.

¹⁸WindShape, “The CAST is now open,” <http://www.windshape.ch/news.html>

¹⁹Perkins, R., “Caltech Launches New Autonomous Systems Research Center,” <http://www.caltech.edu/news/caltech-launches-new-autonomous-systems-research-center-80164>, October 24, 2017.